nature materials

ARTICLES

PUBLISHED ONLINE: 27 MAY 2012 | DOI: 10.1038/NMAT3336

# *In silico* screening of carbon-capture materials

Li-Chiang Lin[1,2†], Adam H. Berger[3†], Richard L. Martin[4†], Jihan Kim[2†], Joseph A. Swisher[1,2], Kuldeep Jariwala[2], Chris H. Rycroft[4,5], Abhoyjit S. Bhown[3], Michael W. Deem[6], Maciej Haranczyk[4] and Berend Smit[1,2,7*]

**One of the main bottlenecks to deploying large-scale carbon dioxide capture and storage (CCS) in power plants is the energy required to separate the $CO_2$ from flue gas. For example, near-term CCS technology applied to coal-fired power plants is projected to reduce the net output of the plant by some 30% and to increase the cost of electricity by 60–80%. Developing capture materials and processes that reduce the parasitic energy imposed by CCS is therefore an important area of research. We have developed a computational approach to rank adsorbents for their performance in CCS. Using this analysis, we have screened hundreds of thousands of zeolite and zeolitic imidazolate framework structures and identified many different structures that have the potential to reduce the parasitic energy of CCS by 30–40% compared with near-term technologies.**

Reducing anthropogenic global $CO_2$ emissions is a complex issue. The scale of the problem, the costs, its interdependence with energy production, and the intrinsic uncertainties in making long-term predictions about something as complex as the climate are a few of the factors contributing to one of the biggest challenges of our time[1]. Despite advances in alternative energy, most, if not all, future energy scenarios include continuing growth in the absolute use of fossil energy[2]. Carbon dioxide capture and storage (CCS), deployed at an industrial scale, is one of the few viable technologies that mitigate anthropogenic $CO_2$ emissions[3]. For power plants, post-combustion CCS involves the separation of $CO_2$ from flue gas, followed by its compression and then sequestration in geological formations. CCS is very energy intensive, and capture dominates both the energy consumption and the cost[3,4].

One can use simple thermodynamics to estimate the minimum energy required to separate $CO_2$ from flue gases (typically, ~75% $N_2$, 12–15% $CO_2$, ~10% $H_2O$, ~3% $O_2$ at 40 °C and 1 atm). If we capture 90% of the $CO_2$ from a coal-fired power plant with the separation performed at 40 °C, the minimum energy required is of the order of 4–5% of the energy produced by the power plant[5]. Near-term capture technologies are projected to use five times this thermodynamic limit[5]. This suggests that capture processes that use less energy may be feasible. The technology for $CO_2$ capture considered near-term for power plants was developed as far back as the 1930s (refs 6,7). This technology uses aqueous solutions of amines that react with $CO_2$ to form carbamates and are therefore highly selective in capturing $CO_2$. One drawback of these amine solutions is that they contain 70% water by weight, and the regeneration cycle involves heating and evaporating large volumes of water, making the process energy intensive. Alternative separation processes that use other solvents, solid adsorbents, or membranes have the potential to require less energy[5]. One of the main challenges here is that many properties of $CO_2$ and $N_2$ are similar, and hence the success of these approaches relies on the development of novel materials sensitive to these small differences.

For adsorbent-based gas separations, it is important to have adsorbents with a large internal surface[8]; examples of such material include zeolites, metal–organic frameworks (MOFs), and zeolitic imidazolate frameworks[9–12] (ZIFs). The number of possible structures of these materials is very large; hundreds of thousands of possible zeolites with different pore topologies exist in the zeolite database[13], and an extremely large number of different types of MOFs can be created by changing the type of the metal and the organic linker. In practical terms, synthesizing and testing all these structures for $CO_2$ separation would be an impossible task. Therefore, we have developed a viable computational strategy to characterize large databases of carbon capture materials and identify optimal materials for $CO_2$ separation.

Several articles on screening for optimal separation materials have been published[14–16]. These articles consider a limited set of 10–20 different materials, which is insufficient to characterize the hundreds of thousands of different possible topologies[13]. Moreover, these studies often focus on a single material property, such as selectivity or breakthrough time, at a specific condition. However, optimizing the breakthrough time[15] or uptake[16] in the adsorption step, for example, ignores that a material effective at adsorbing $CO_2$ might be difficult to regenerate. More importantly, these studies do not consider that different materials perform optimally at different conditions. In this work, we take another approach. For each material, we determine the optimal process conditions by minimizing the electric load imposed on a power plant by a temperature–pressure swing capture process using that material followed by compression. This minimum load, which we call parasitic energy, is introduced as a metric to compare different materials.

Separation of gases using nanoporous materials exploits the fact that at flue gas conditions, $CO_2$ selectively adsorbs in the pores of these materials. By increasing the temperature, decreasing the pressure, or a combination of both, nearly pure $CO_2$ can be recovered. Figure 1 illustrates such a temperature–pressure swing separation process. Regardless of the regeneration method, the

[1]Department of Chemical and Biomolecular Engineering, University of California, Berkeley, California 94720-1462, USA, [2]Materials Science Division, Lawrence Berkeley National Laboratory, Berkeley, California 94720, USA, [3]Electric Power Research Institute (EPRI), 3420 Hillview Avenue, Palo Alto, California 94304, USA, [4]Computational Research Division, Lawrence Berkeley National Laboratory, Berkeley, California 94720-8139, USA, [5]Department of Mathematics, University of California, Berkeley, California 94720, USA, [6]Departments of Bioengineering and Physics and Astronomy, Rice University, Houston, Texas 77005, USA, [7]Department of Chemistry, University of California, Berkeley, California 94720-1462, USA. †These authors contributed equally to this work. *e-mail: bsmit@lbl.gov.

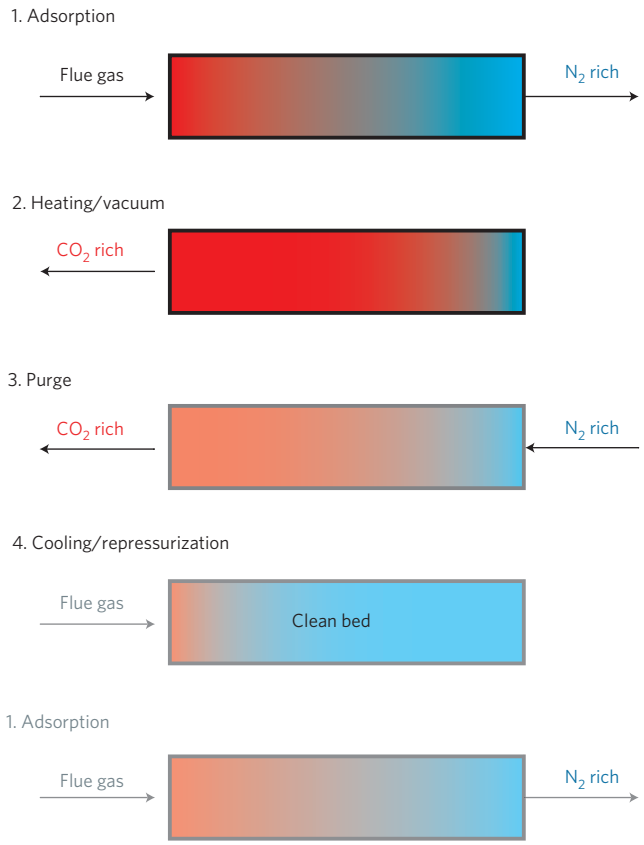


**Figure 1 | Hybrid pressure and temperature swing adsorption.** In the adsorption step (1) the flue gas is brought into contact with the solid adsorbent. The material selectively adsorbs $CO_2$ and (nearly) pure $N_2$ leaves the adsorber. When the adsorber is saturated, it is regenerated (2) by heating the system and/or applying a vacuum. The purge (3) and cooling or repressurization step (4) brings the system back to its original state (1). The amount of $CO_2$ that is removed from the flue gas in a single cycle defines the working capacity of a material. The regenerated $CO_2$ is subsequently pressurized to 150 bar for geological storage.

parasitic energy of a CCS process can be readily modelled if equilibrium adsorption and desorption are assumed. Although there are many possible process configurations, they all rely on the difference between adsorption and desorption conditions to capture $CO_2$. The processes vary primarily in their method of gas-solid contacting and heat transfer, although neither of those factors affects performance under equilibrium assumptions. The energy required for this process has three main components: (1) energy to heat the material, (2) energy to supply the heat of desorption (equal to the heat of adsorption), and (3) energy required to pressurize $CO_2$ to 150 bar, which is a standard requirement for transport and storage[4]. For a specific material and a fixed adsorption condition, we vary the desorption conditions and calculate the $CO_2$ and $N_2$ loading differential between the adsorption and desorption conditions to compute the quantity and purity of $CO_2$ captured. The thermal energy requirement ($Q$) of the process per unit mass of $CO_2$ captured ($m_{CO_2}$) is the sum of the sensible energy needed to heat the bed to the desorption temperature and the energy needed to supply the heat of adsorption.

$$Q = \frac{C_p m_{sorbent}(T_{final} - T_{flue}) + (\Delta q_{CO_2} \Delta h_{CO_2} + \Delta q_{N_2} \Delta h_{N_2})}{m_{CO_2}}$$

where $C_p$ is the specific heat capacity of the adsorbent, $m_{sorbent}$ is the mass of the adsorbent, $T_{final} - T_{flue}$ is the temperature differential between the adsorption and desorption conditions, $\Delta q_i$ is the difference in loading and $\Delta h_i$ is the heat of adsorption for each species. The loading at specific conditions is calculated using competitive adsorption isotherms, and the heats of adsorption are obtained directly from the molecular simulations. In a power plant, this thermal energy is supplied by diverting steam from the power cycle. Diverting steam effectively imposes a parasitic load on the power plant, which we compute as the product of the thermal energy requirement ($Q$), the Carnot efficiency ($\eta$) of the extracted steam, and the typical efficiency of a turbine (75%; ref. 17). The compressor work, $W_{comp}$, is obtained from a multi-stage intercooled compressor model with real gas properties using NIST REFPROP (ref. 18) for fluid property data. We assume a staged compression, intercooled to 40 °C, with a maximum pressure ratio of 2.5 and an isentropic efficiency of 85% below the supercritical point and 90% above it. Finally, the parasitic energy, $E_{eq}$, imposed on the power plant of the CCS process, is given by:

$$E_{eq} = 0.75\eta_{T_{final}} Q + W_{comp}$$

For each material we find the optimal process conditions by minimizing this parasitic energy. Using a similar analysis, a state-of-the-art amine capture process would have a parasitic energy of 1,060 kJ $(kg\,CO_2)^{-1}$. A more rigorous engineering analysis of an amine process retrofitted to a coal-fired power plant, including the pressure drop through equipment, losses in heat exchangers, and other energy losses, shows a parasitic load of 1,327 kJ $(kg\,CO_2)^{-1}$, about 25% higher[4]. Therefore, we seek materials that exhibit a parasitic energy significantly lower than 1,060 kJ $(kg\,CO_2)^{-1}$ with the expectation that, similar to the amine process, a more detailed analysis of a process attached to a power plant will increase this number. We also emphasize that for the present analysis we treat the flue gas as a binary gas mixture of 14% $CO_2$ and 86% $N_2$. This assumption allows us to focus first on the energy consumption of these materials. If the energy consumption looks sufficiently attractive relative to other processes, further criteria such as sensitivity to other flue gas components (for example, $H_2O$, $SO_x$, $NO_x$), as well as cost, attrition, stability, and availability can be examined.

To determine the minimum parasitic energy of a material, the most important data are the (mixture) adsorption isotherms. As the experimental adsorption isotherms are known for very few materials, we rely on molecular simulation to predict these isotherms for the different materials. Conventional grand canonical Monte Carlo (GCMC) simulations allow us to predict a complete isotherm on the basis of the crystal structure of the material[19,20]. These simulations, however, require on the order of days of central processor unit (CPU) time, which is prohibitively slow to screen hundreds of thousands of materials. To obtain adsorption isotherms in a high-throughput manner, we have developed an efficient algorithm that allows us to obtain a complete isotherm in a few seconds on a graphics processing unit (GPU). Our method relies on the observation that pure component adsorption isotherms in these materials can be accurately described using dual- or single-site Langmuir isotherms[21]:

$$q_i = \sum_{j=1}^{N} \frac{K_{i,j} P_i}{1 + \frac{K_{i,j}}{q_{sat,i,j}} P_i}$$

where $q_i$ is the loading at the partial pressure $P_i$ of the component $i$, $K_{i,j}$ is the Henry coefficient, and $q_{sat,i,j}$ is the saturation loading of the component $i$ corresponding to adsorption site $j$. In our model, only the single-site ($N$ equal to 1) isotherm was adopted for $N_2$ whereas either single- or dual-site ($N$ equal to 2) isotherms were applied for $CO_2$. The temperature dependence of the Henry coefficients follows directly from the heats of adsorption, both of which were

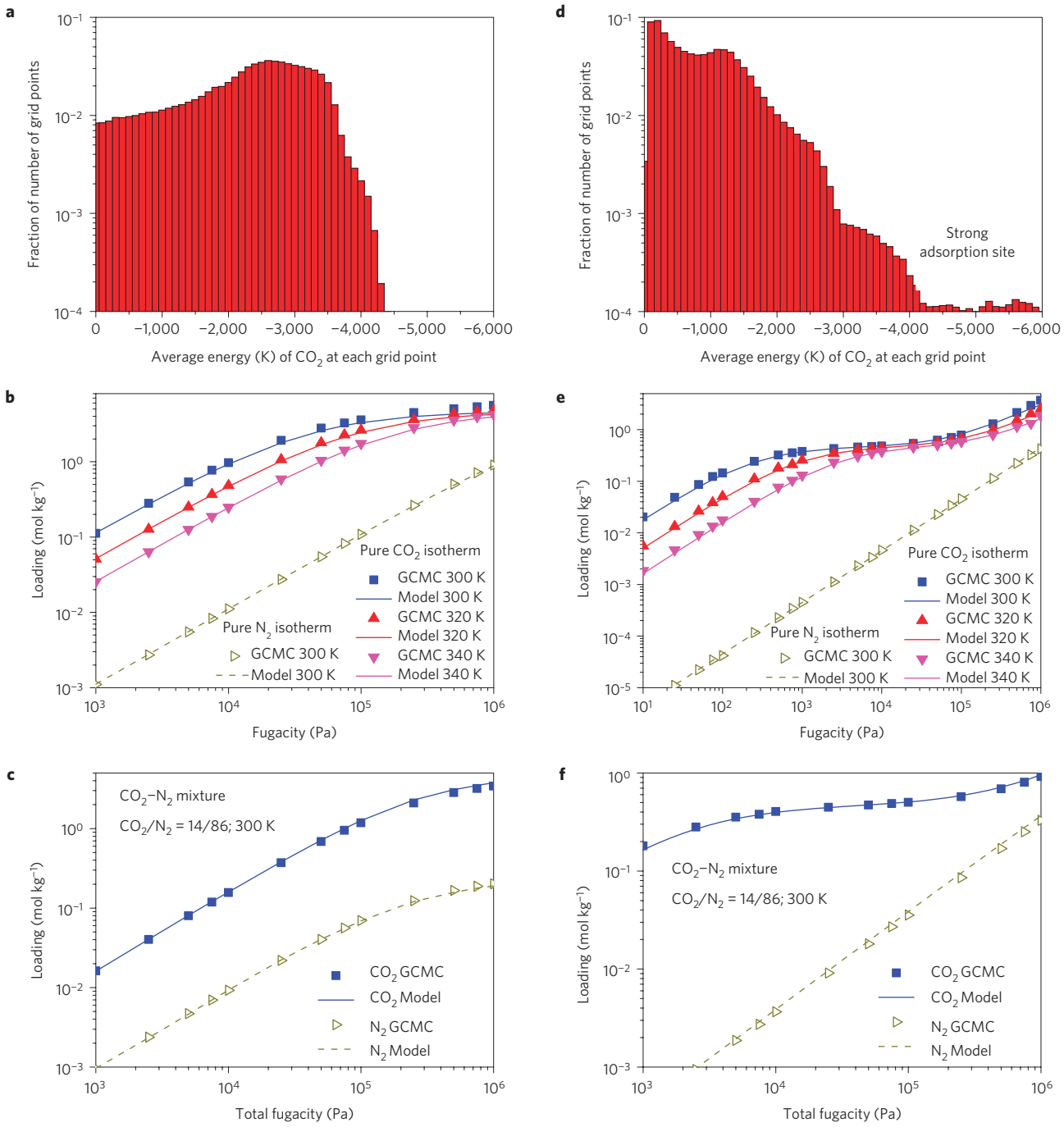


**Figure 2 | (Mixture) adsorption isotherms. a–f**, Probability distribution of the energies of a particle inserted in the pores (**a**,**d**) pure component isotherms for $CO_2$ and $N_2$ and pure $CO_2$ isotherms at different temperatures (**b**,**e**) and mixture isotherms (**c**,**f**) for two materials: the zeolite SIV (**a**–**c**) and the predicted zeolite PCOD8286959 (**d**–**f**). The symbols are the results from the GCMC simulations and the lines are the results of our methodology using the GPU calculations.

obtained from molecular simulations. The total saturation loading of the pure component gas was calculated using a correlation of guest molecule density in the framework to pore diameter. For $CO_2$ adsorption, the use of dual-site isotherms is required for structures that contain particularly strong adsorption sites; this behaviour arises because $CO_2$ first adsorbs at these sites, and only once all these positions are saturated does it absorb in the rest of the material. Figure 2a,d illustrate the difference between materials best described by single-site and dual-site isotherms, respectively. The long tail at low energies in the energy distribution is a signature of the presence of these strong adsorption sites. If such a signature exists, we use a dual-site description; otherwise, the isotherms are described using a single site. Figure 2e shows a typical case of such a dual site isotherm for pure $CO_2$. One observes a plateau in the isotherm at low pressure, which results from the saturation of the strong adsorption sites. Each strong adsorption site can generally accommodate only one $CO_2$ molecule, so the saturation loading for these sites is just the sum of the number of unique sites. We have developed an automated algorithm to identify the presence of these sites during molecular simulation and accordingly divide the structure into two regions, computing their own associated Henry coefficients, heats of adsorption, and saturation loadings.

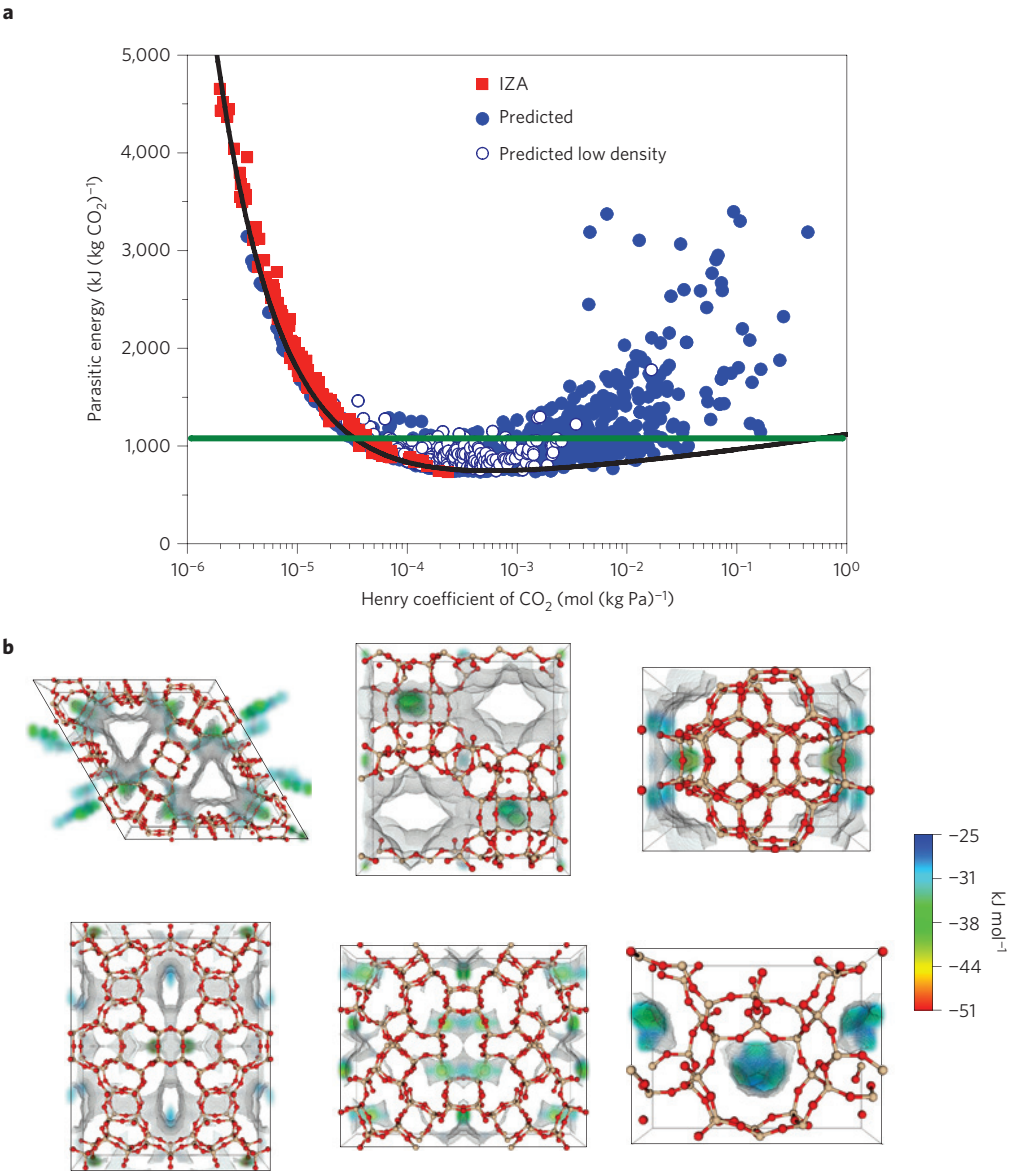


**Figure 3 | Parasitic energy as a function of the Henry coefficient of $CO_2$ for all silica zeolite structures. a**,**b**, The Henry coefficient can be obtained from the adsorption isotherm; at sufficiently low pressure the Henry coefficient multiplied by the pressure gives the number of adsorbed molecules. In **a** we compare the IZA zeolite structures (red squares) with the predicted structures (blue circles). The open blue circles are computationally predicted structures near the low-density feasibility line, which are most likely to be synthesizable. The green line gives the parasitic energy of the current monoethanolamine (MEA) technology, and the black line is the minimal parasitic energy observed for a given value of the Henry coefficient in the all-silica structures. In the Supplementary Information we show the sensitivity of the parasitic energy to uncertainties in our parameters. In this graph, we plotted a representative fraction of all structures. More data can be found at www.carboncapturematerials.org. On the website, every data point can also be linked to a structure. **b** gives some examples of the optimal all-silica structures; out of the fifty top performing materials we selected the six most diverse. The figures show the atoms of materials as ball and stick (O, red; Si, tan). The surface gives the local free energies in the pores of the material, where warmer colours indicate the dominant $CO_2$ adsorption sites.

Figure 2b,e demonstrate that our model is able to predict the correct temperature dependence of the pure component isotherms.

The most commonly used method to predict mixture adsorption isotherms is ideal adsorbed solution theory[22]. However, as carbon capture of flue gases occurs at relatively low pressure, competitive Langmuir isotherms give an equally good description. If a dual-site model for $CO_2$ is used, we assume that $N_2$ is not able to compete with $CO_2$ at the stronger adsorption site, and take the saturation value for $N_2$ to be the same as $CO_2$ outside of the strong adsorption region, which is required for consistency with the assumption of the competitive adsorption isotherm[23]. To test the reliability of the competitive Langmuir model in predicting the mixture isotherms on the basis of the pure components, we used the GCMC simulated mixture adsorption isotherms as 'experimental data' to test whether the Langmuir model correctly predicts these mixture isotherms given the predicted pure component isotherms. We have tested over 50 different structures and, for all systems, the competitive model accurately reproduces the mixture isotherms over a large range of pressures, including the partial pressures relevant for flue gas separations. Figure 2c,f demonstrate the performance of the competitive isotherm model with the corresponding GCMC simulations (see Supplementary Information for the other structures).

Figure 3a shows the optimized parasitic energy as a function of the $CO_2$ Henry coefficient for all known zeolite structures. For these

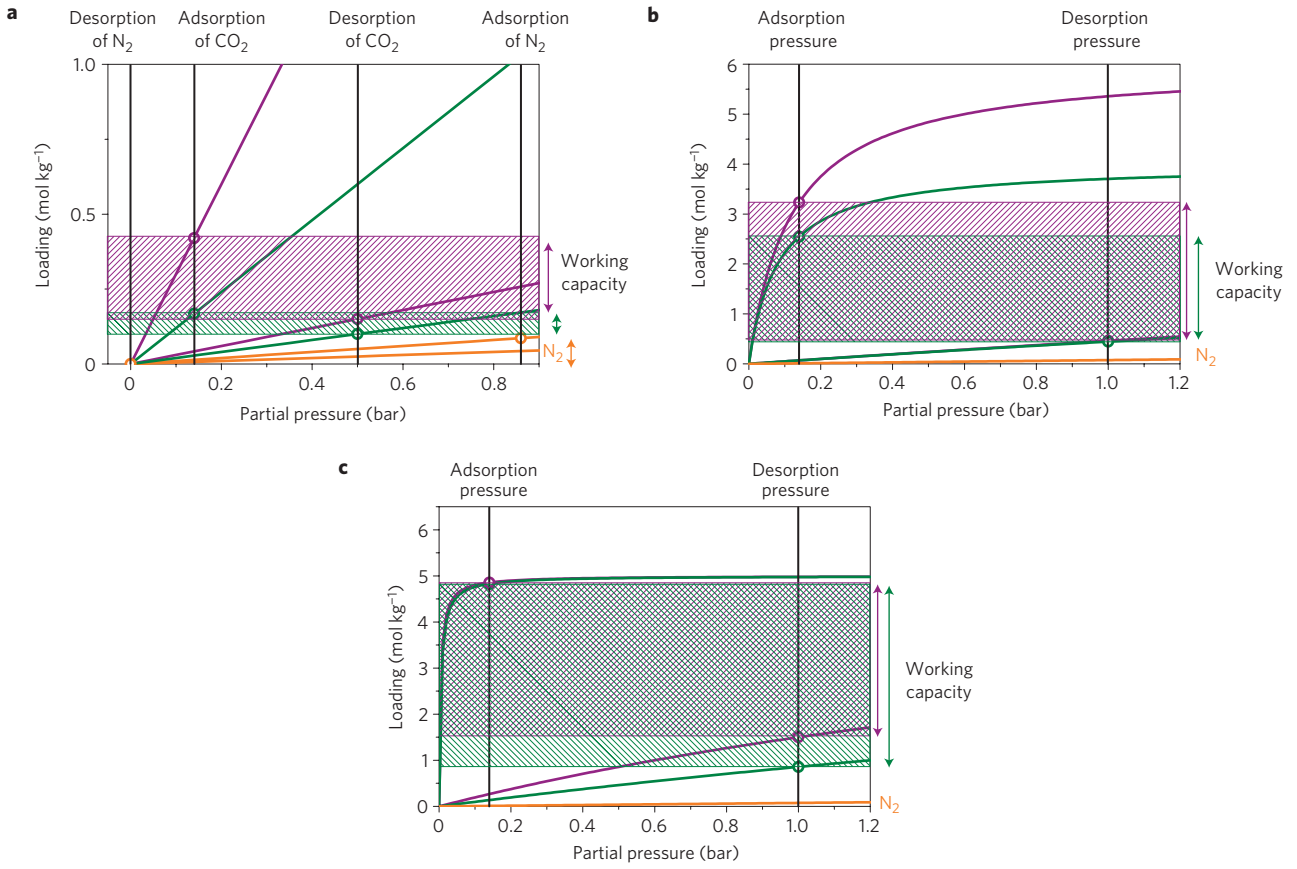


**Figure 4 | Adsorption isotherms.** The loading in the zeolite is plotted as a function of the partial pressure of $CO_2$ (green or purple) or $N_2$ (orange). Adsorption is set by the flue gas conditions (40 °C, 1 atm and 14% $CO_2$ and 86% $N_2$) and the desorption is at a temperature $T_{final}$. The working capacity follows from the difference in the amount of adsorbed $CO_2$ at adsorption and desorption conditions. In most of these materials the $N_2$ adsorption is so small that it does not contribute much to the parasitic energy, and only for materials where the adsorption of $CO_2$ is equally small do we consider the contribution of $N_2$. At sufficiently low pressure, these adsorption isotherms are linearly related to the pressure, with the proportionality constant defined as the Henry coefficient. **a**, A material for which the Henry coefficient is sufficiently low such that both the adsorption and desorption are in the Henry regime. A low Henry coefficient (green) gives a relatively small working capacity and purity of the product stream. Increasing the Henry coefficient (purple) gives a significant increase of the working capacity. **b**, If the Henry coefficient becomes much larger, the number of adsorbed $CO_2$ molecules is so large that $CO_2$–$CO_2$ interactions in the materials are important at the partial pressure of $CO_2$ corresponding to flue gas conditions. Hence, the adsorption cannot be characterized with a Henry coefficient only. **c**, For those materials with a very high Henry coefficient, a further increase of the Henry coefficient will have little effect on the uptake value at adsorption, as this is now dominated by the pore volume. For desorption, however, increasing the Henry coefficient will further decrease the working capacity. For **b** and **c**, as desorption occurs at higher temperatures, the desorption pressure is still in the Henry regime.

materials we observe a monotonically decreasing parasitic energy as a function of the Henry coefficient. To investigate the lowest parasitic energy that can be obtained using these materials, we perform calculations on a database containing over three hundred thousand predicted zeolite structures[13]. These calculations identify predicted structures with parasitic energies that are lower than can be obtained for the known structures. Figure 3b shows some of the structures that have near-optimal parasitic energy.

The parasitic energy as a function of the Henry coefficient shows three regimes. The mixture isotherms in these regimes are shown schematically in Fig. 4. Adsorption of $CO_2$ takes place at flue gas conditions (1 atm and 40 °C). The subsequent desorption is achieved by decreasing the (partial) pressure and/or increasing the temperature. The difference in $CO_2$ concentration between adsorption and desorption defines the working capacity of a material and gives the amount of $CO_2$ that is removed in an adsorption cycle. For materials with a small Henry coefficient (Fig. 4a), the performance is poor because the working capacity is small, yet the entire system needs to be heated to the desorption conditions, giving a high parasitic energy. Furthermore, the adsorption of $CO_2$ is of the same order of magnitude as $N_2$ in these materials and hence the selectivity of such a material is unusably low. Materials with a larger Henry coefficient have a significantly larger working capacity and correspondingly lower parasitic energy. This trend continues until the Henry coefficient of the material is so large that at flue gas conditions the pressure is too high for the $CO_2$ adsorption to be in the linear regime. Figure 4b shows that at these conditions the $CO_2$ loading at the adsorbed state is no longer fully determined by the Henry coefficient, and that materials with the same Henry coefficient have different working capacities, depending on the pore volume. Figure 4c illustrates that at even larger Henry coefficients the adsorption of $CO_2$ becomes so strong that it becomes increasingly difficult to regenerate the material. Another important observation is that we have a broad optimum. The reason for this broad minimum is that the Henry coefficient shows a strong correlation with the heat of adsorption, and the heat of adsorption makes two opposing contributions to the parasitic energy. As the temperature dependence of the Henry coefficient is proportional to the heat of adsorption, a higher heat of adsorption increases the working capacity. Although this reduces the parasitic energy, it is offset by the requirement to supply more energy to desorb $CO_2$, which again increases the parasitic energy.

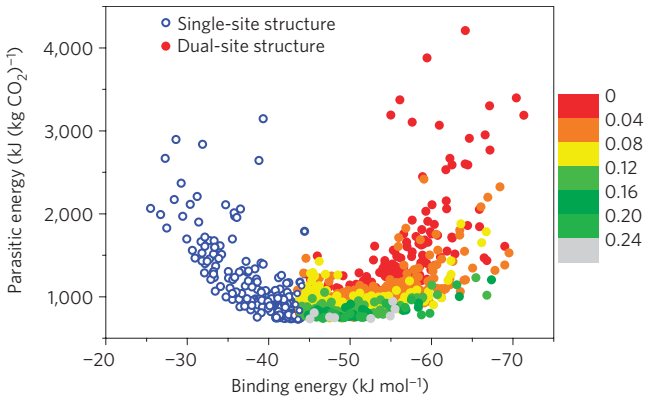


**Figure 5 | Optimal materials.** The parasitic energy as a function of the binding energy for a $CO_2$ molecule. The binding energy is defined as the lowest energy that can be observed in a given structure. If this binding is sufficiently strong, dual-site adsorption behaviour will arise. The fraction of each material's volume which is occupied by low-energy strong adsorption sites is displayed as coloured solid circles. The colour bar gives the volume fraction of these low-energy regions. Structures without these specific features (that is, single site adsorption behaviour) are displayed as open blue circles.

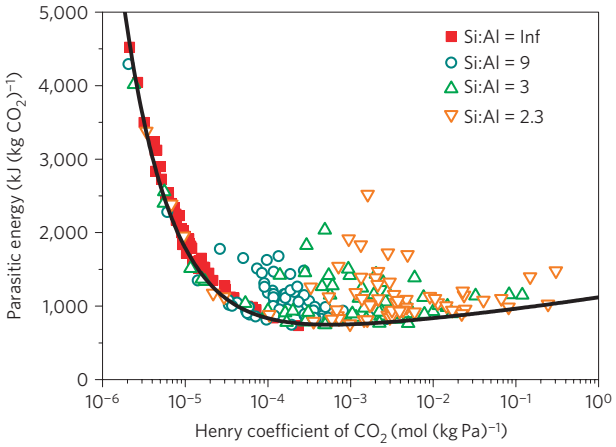


**Figure 6 | Parasitic energy for zeolites with cations.** The parasitic energy as a function of the $CO_2$ Henry coefficient for known zeolite structures with different Al/Si ratios. The all-silica IZA structures are shown as red squares and the corresponding structures with different cation concentrations are labelled as indicated by open symbols.

Our screening shows a large set of zeolite structures which have a parasitic energy well below the current technology 1,060 kJ $(kg\,CO_2)^{-1}$. Inspection of these optimal structures highlights their diversity: we find one-, two-, and three-dimensional channel structures, cage-like topologies, and more complex geometries. To illustrate this point we show in Fig. 3b a diverse sample of structures[24] contained in the set of optimal zeolites. It is interesting to compare these with the optimal known zeolite structures in Fig. 3a. Several of the known zeolite structures have a sufficiently low parasitic energy; however, most of these known structures are one-dimensional channels, which may suffer from severe diffusion limitations[14]. By contrast, many of the predicted zeolite structures have adsorption sites, where $CO_2$ strongly adsorbs along channels with larger diameters. Transport of $CO_2$ to and from the sites of adsorption occurs via the larger channels, so diffusion is not expected to be a limiting factor. Interestingly, none of the known zeolites have this characteristic feature, and we consider this observation to be a significant discovery. This discovery was facilitated through the screening of an exhaustive number of possible topologies.

A common feature of most optimal materials is a set of local regions of the structure that bind $CO_2$ preferentially, leading to dual-site adsorption behaviour. Figure 5 shows the parasitic energy as a function of the binding energy of a $CO_2$ molecule. To this figure we added those materials that have (near) optimal Henry coefficients, but without such dual-site behaviour, which includes some of the known zeolite structures. We observe a similar correlation with the Henry coefficient, because the binding energy dominates the Henry coefficient for structures with these preferential sites. The binding energy needs to be optimal: too low and the material adsorbs too little $CO_2$, too high and the material becomes too difficult to regenerate. Figure 5 further shows that the parasitic energy is influenced by the density of strong adsorption sites in the material; the optimal materials exhibit the largest number of strong adsorption sites per unit volume. This observation is important as it explains why these materials exhibit a lower limit for the parasitic energy. The existence of a strong adsorption site requires a minimum amount of zeolite material, which, combined with the size of a $CO_2$ molecule, gives an upper limit to the total number of such local regions that can exist per unit volume.

An important practical question is whether we can synthesize these optimal materials. As the synthesis conditions of the known zeolites favour the formation of low-density structures[25], one expects that among the predicted structures these low-density structures are the most likely ones to be synthesized. As highlighted in Fig. 3a, this subset indeed has many structures with optimal performance. Recent developments[26] in novel structure directing agents may make it possible to synthesize some of these structures.

An alternative strategy to create optimal Henry coefficients is to synthesize zeolites with different Al:Si ratios. In aluminosilicate zeolites, cations are present in the pores to compensate for the charge imbalance introduced by the $Al^{3+}$ that replaces a $Si^{4+}$. Figure 6 shows the effect of cations on the parasitic energy for the known zeolites for different Al:Si ratios. Cations create adsorption sites for $CO_2$ but also reduce the pore volume. The net result on the parasitic energy of these two effects depends on the particular structure. The addition of cations to low Henry coefficient structures causes a decrease in the parasitic energy due to the increased number of adsorption sites; however, the additional cations eventually increase the parasitic energy as the pore volume decreases. In contrast, addition of cations to near-optimal Henry coefficient structures increases the parasitic energy because the decrease in pore volume dominates. It is important to stress that every structure has its own optimal Al:Si ratio. Comparison with the parasitic energy for the all-silica structures shows that the addition of cations does not yield a material that has a lower parasitic energy for the same Henry coefficient. This observation is consistent with the notion that one has to create an adsorption site with exactly the right adsorption strength and that there is a limit to the maximum number of adsorption sites per unit volume.

Figure 7a shows the parasitic energy for ZIFs. For these materials, the overall parasitic energy is higher than for zeolites. As we have focused on the simplest linker (imidazole), the selectivity towards $CO_2$ is rather low: linkers with higher selectivity will increase the Henry coefficient to a more optimal value and reduce the parasitic energy. Figure 7b gives a set of optimal ZIF structures. These structures look very different from the optimal zeolite structures; optimal ZIFs are those in which there are channels where $CO_2$ can access the non-hydrogen atoms of the structure.

There are important experimental consequences to our results. Our metric provides a direct insight into the overall performance of a material in an actual carbon capture process. In this context, it is instructive to compare our metric with the recently proposed

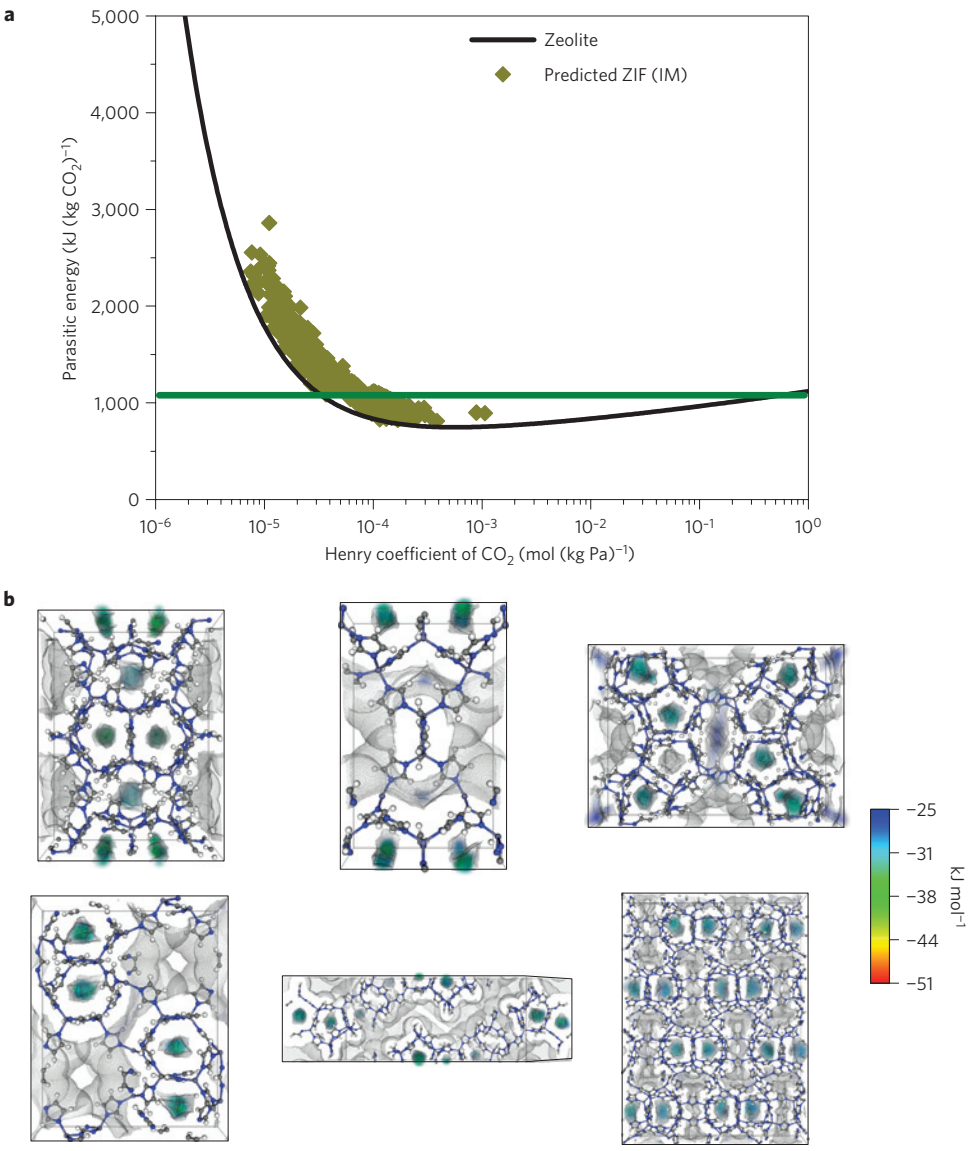


**Figure 7 | Parasitic energy for ZIFs. a**, The parasitic energy as a function of the $CO_2$ Henry coefficient for ZIFs is shown. The green lines give the parasitic energy of the current MEA technology, and the black line is the minimal parasitic energy calculated for a given value of the Henry coefficient in the all-silica structures. In this graph, we plotted a representative fraction of all structures. More data can be found at www.carboncapturematerials.org. On the website, every data point can also be linked to a structure. **b**, Out of the fifty top performing ZIFs, we selected the six most diverse. The figures show the atoms of materials as ball and stick models (Zn, blue-grey; N, blue; H, white; C, grey). The surface gives the local free energies in the pores of the material.

alternative metric based on the adsorption breakthrough time[15]. Materials with a higher Henry coefficient, for a given saturation loading, will give a longer breakthrough time. However, as this study shows, materials with extremely high Henry coefficients perform poorly because the regeneration step cannot be ignored in a carbon capture process. This illustrates the limitation of focusing on a single material property rather than the entire process.

Our screening establishes a theoretical limit for the minimal parasitic energy that can be achieved for a class of materials. Such a target will be useful to focus experimental efforts to synthesize such materials. Our screening provides for each class of materials a unique structure that gives the best performance. However, from a practical point of view, 1–3% higher parasitic energies will not make a difference. To have many near optimal structures is very important as it increases the chances one of these structures can be synthesized. To facilitate this synthesis effort, all of these structures, together with all physical properties that lead to the increase in performance, are available online[27].

A specific outcome of our study is that an optimal carbon capture material has a sufficient number of adsorption sites with a binding energy that is sufficiently large to be selective, but not so large that it becomes difficult to desorb. This is a very general conclusion and explains why our parasitic energy curve holds for all the materials we have studied. This parasitic energy curve can be used as a reference to benchmark other materials.

## Methods

As most of the materials experimental data do not exist, we use molecular simulations to predict the adsorption isotherms. As input, these simulations require the crystal structure of the materials and a force field describing the interactions. In addition, by accelerating computationally expensive steps in molecular simulation using GPUs, we enable screening of materials in a high-throughput manner.

**Crystal structures.** For the all-silica zeolite structures, we used the experimental zeolite crystal structures[28] and the database with predicted, fully optimized zeolite crystal structures[13,25]. This database was constructed by searching the chemical space of possible $SiO_2$ structures that are zeolite-like. This was done by examining

all 230 space groups and a wide range of unit cell dimensions and silicon densities. Symmetry operations acting on crystalographically unique atoms were used to generate the full unit cell structure. A Monte Carlo procedure was used to sample this vast space of possibilities, giving 2.6 million topologically distinct zeolite-like structures. These structures were optimized by detailed interatomic potentials[29,30]. Depending on the force field, 330,000–590,000 of these structures are thermodynamically accessible, with energies 0–30 kJ $mol^{-1}$-Si above α-quartz. Of these structures we only considered those with pores with a diameter sufficiently large (above 3.25 Å) for $CO_2$ to enter[31]. The structures in this database have topological, geometrical, and diffraction characteristics that are similar to those of known zeolites[13,25].

In most zeolites the Si can be exchanged with Al, which creates a charge deficit that is compensated by cations (for example, $Na^+$, $H^+$, $Ca^{2+}$). The location of these Al sites is known only for a limited number of structures[20,32]. A reasonable starting point[20] is to assume a random distribution of Al over the T sites such that Loewenstein's rule[33] is obeyed, which implies a maximum Al/Si ratio of one. For this ratio and for Al/Si equal to zero we have one unique structure. For the other Al/Si ratios there are many different possible distributions of the Al atoms over the T sites. For these ratios we generated at least ten different Al atom distributions and the cations were subsequently added at the minimum energy positions[34]. Each distribution can have a slightly different adsorption isotherm and we averaged the parasitic energy[32]. In addition, we compared the results for systems in which the cations were fixed at the minimum energy configurations, with simulations in which the cations were free to move. For structures with a low Henry coefficient, we found a lower parasitic energy compared with a system with moving cations. For those structures with optimal Henry coefficients, these differences were negligible.

ZIFs are a class of MOFs that have a pore topology that is isomorphic with the zeolite structures[12,35]. In ZIFs transition metal atoms (M) replace the Si atoms and imidazolates (IM) replace bridging oxides in zeolites. Given that the M–IM–M angle is similar to the Si–O–Si angle, ZIFs form 3D networks with topologies that are similar to zeolites. We applied this analogy to the zeolite database to generate ZIFs using the ZEO++ code[31]. In the reported zinc and IM-based ZIFs with International Zeolite Association (IZA) zeolite topologies[35] the distance between zinc atoms and the centre of IM rings is about 1.95 times larger than the Si–O distance in zeolites. A ZIF structure was generated by scaling the unit cell of the corresponding zeolite structure by the same factor and exchanging each oxygen atom with an IM group and each Si atom with a Zn atom. We have validated the resulting ZIF geometries by comparing geometries of two structures for which the experimental geometries are known: ZIF-3 (the DFT topology) and ZIF-10 (the MER topology). The observed differences in the geometries do not translate into significant differences in the parasitic energy.

**Model and simulation details.** Calero and co-workers[36,37] have developed a force field that accurately reproduces the experimental isotherms in zeolites. For ZIFs, parameters for the framework atoms were taken from the DREIDING force field[38] and parameters for $CO_2$ and $N_2$ were taken from the TraPPE force field[39]. Framework-molecule interaction parameters were calculated using the Lorentz–Berthelot mixing rules. Partial charges for ZIF atoms were computed using the connectivity based approach of Zhong and Xu[40]. Adsorption isotherms were calculated using GCMC (ref. 19). The experimental equations of state are used to convert the chemical potentials into (partial) pressures.

**GPU calculations.** To screen a large number of zeolite and ZIF structures we developed a GPU code to accelerate the molecular simulations. We focus on computing the Henry coefficients and the heats of adsorption. The algorithm is divided into three different routines: energy grid construction, pocket blocking, and Widom test particle insertion.

Energy grid construction. To save computational time we construct a grid, giving the energies of the atoms at the grid positions in the unit cell of a framework[20]. The energy grid has a mesh size of 0.1 Å and the interaction between the gas molecule and all of the framework atoms is modelled by the Lennard-Jones potential and the Coulomb potential, with Ewald summations used to calculate the latter. Each of the grid points maps to a single Compute Unified Device Architecture (CUDA) thread and the pairwise potentials are computed in parallel across different CUDA blocks[41]. The positions of the framework atoms are put inside the fast constant memory in the GPU to expedite calculations. At the end of the routine, the array that contains the energy values is transferred from the GPU to the CPU as an input to the pocket blocking routine.

Pocket blocking. In a GCMC simulation, one can insert molecules in pockets that are inaccessible from the outside[42]. The void space analysis algorithm[43] is used to detect and block these inaccessible pockets[44]. We use the values from the energy grid to determine the accessibility of a particular configuration/point in the unit cell using the (multicore) CPU, as this routine does not map well to the GPU architecture. The discrete energy grid is mapped to a binary grid of accessible/inaccessible points on the basis of a certain threshold value that is chosen to be large enough such that on an experimental timescale the pocket is considered inaccessible. Finally, we use a parallel flood fill algorithm to segment the grid into connected, accessible regions. These regions are then classified as either channels or inaccessible pockets, and we set all grid points inside pockets to a very high energy value.

Widom test particle insertion. Using this revised energy grid, we can calculate both the Henry coefficients and the heats of adsorption using Widom insertion moves[19]. We randomly insert a guest molecule inside the simulation box and calculate both the Boltzmann factor and the energy for the particular guest molecule configuration. We can use interpolating functions to estimate the energy values at points that are not directly on the grid. In the GPU architecture, each CUDA thread can conduct independent Widom insertions.

Overall, most of the computational time is spent in the GPU energy grid construction routine. In this routine, there is roughly a factor of 50 in performance improvement going to the GPU (Tesla C2050 Fermi) from the CPU (single core of a 2.4 GHz Intel 5530 Xeon).

Received 11 October 2011; accepted 18 April 2012; published online 27 May 2012

## References


1. Chu, S. Carbon capture and sequestration. *Science* **325,** 1599 (2009).
2. Pacala, S. & Socolow, R. Stabilization wedges: Solving the climate problem for the next 50 years with current technologies. *Science* **305,** 968–972 (2004).
3. Metz, B., Davidson, O., deConinck, H., Loos, M. & Meyer, L. *IPCC Special Report on Carbon Dioxide Capture and Storage*. (Intergovernmental Panel on Climate Change (IPCC), 2005); http://www.ipcc.ch.
4. Massood, R., Timothy, J. S., Nsakala ya, N. & Liljedahl, G. N. *Carbon Dioxide Capture from Existing Coal-Fired Power Plants* (National Energy Technology Laboratory, US Department of Energy, 2007).
5. Bhown, A. S. & Freeman, B. C. Analysis and status of post-combustion carbon dioxide capture technologies. *Environ. Sci. Technol.* **45,** 8624–8632 (2011).
6. Bottoms, R. Separating acid gases. US Patent 1,783,901 (1930).
7. Rochelle, G. T. Amine scrubbing for $CO_2$ capture. *Science* **325,** 1652–1654 (2009).
8. Ciferno, J. P., Marano, J. J. & Munson, R. K. Technology integration challenges. *Chem. Eng. Prog.* **107,** 34–44 (2011).
9. Ferey, G. Hybrid porous solids: Past, present, future. *Chem. Soc. Rev.* **37,** 191–214 (2008).
10. Yaghi, O. M. *et al.* Recticular synthesis and the design of new materials. *Nature* **423,** 708–714 (2003).
11. D'Alessandro, D. M., Smit, B. & Long, J. R. Carbon dioxide capture: Prospects for new materials. *Angew. Chem. Int. Ed.* **49,** 6058–6082 (2010).
12. Banerjee, R. *et al.* High-throughput synthesis of zeolitic imidazolate frameworks and application to $CO_2$ capture. *Science* **319,** 939–943 (2008).
13. Deem, M. W., Pophale, R. & Cheeseman, P. A. A database of new zeolite-like materials. *Phys. Chem. Chem. Phys.* **13,** 12407–12412 (2011).
14. Krishna, R. & van Baten, J. M. *In silico* screening of metal-organic frameworks in separation applications. *Phys. Chem. Chem. Phys.* **13,** 10593–10616 (2011).
15. Krishna, R. & Long, J. R. Screening metal-organic frameworks by analysis of transient breakthrough of gas mixtures in a fixed bed adsorber. *J. Phys. Chem. C* **115,** 12941–12950 (2011).
16. Yazaydin, A. O. *et al.* Screening of metal-organic frameworks for carbon dioxide capture from flue gas using a combined experimental and modeling approach. *J. Am. Chem. Soc.* **131,** 18198 (2009).
17. Freeman, S. A., Dugas, R., Van Wagener, D., Nguyen, T. & Rochelle, G. T. Carbon dioxide capture with concentrated, aqueous piperazine. *Energy Procedia* **1,** 1489–1496 (2009).
18. Lemmon, E. W., Huber, M. L. & McLinden, M. O. NIST Reference Fluid Thermodynamic and Transport Properties Database (REFPROP): Version 9.0. (NIST, 2010); http://www.nist.gov/srd/nist23.cfm.
19. Frenkel, D. & Smit, B. *Understanding Molecular Simulations: From Algorithms to Applications* 2nd edn (Academic, 2002).
20. Smit, B. & Maesen, T. L. M. Molecular simulations of zeolites: Adsorption, diffusion, and shape selectivity. *Chem. Rev.* **108,** 4125–4184 (2008).
21. Krishna, R., Calero, S. & Smit, B. Investigation of entropy effects during sorption of mixtures of alkanes in MFI zeolite. *Chem. Eng. J.* **88,** 81–94 (2002).
22. Myers, A. L. & Prausnitz, J. M. Thermodynamics of mixed gas adsorption. *Am. Inst. Chem. Eng. J.* **11,** 121–130 (1965).
23. Rao, M. B. & Sircar, S. Thermodynamic consistency for binary gas adsorption equilibria. *Langmuir* **15,** 7258–7267 (1999).
24. Martin, R. L., Smit, B. & Haranczyk, M. Addressing challenges of identifying geometrically diverse sets of crystalline porous materials. *J. Chem. Inf. Modell.* **52,** 308–318 (2012).
25. Deem, M. W., Pophale, R., Cheeseman, P. A. & Earl, D. J. Computational discovery of new zeolite-like materials. *J. Phys. Chem. C* **113,** 21353–21360 (2009).
26. Simancas, R. *et al.* Modular organic structure-directing agents for the synthesis of zeolites. *Science* **330,** 1219–1222 (2010).
27. Jariwala, K. & Haranczyk, M. http://www.carboncapturematerials.org (2011).
28. International Zeolite Association (IZA); http://www.iza-structure.org/databases (2011).
29. Sanders, M. J., Leslie, M. & Catlow, C. R. A. Interatomic potentials for $SiO_2$. *J. Chem. Soc. Chem. Commun.* 1271–1273 (1984).

30. Beest, B. W. H. v., Kramer, G. J. & Santen, R. A. v. Force fields for silicas and aluminophosphates based on *ab initio* calculations. *Phys. Rev. Lett.* **64,** 1955–1958 (1990).
31. Willems, T. F., Rycroft, C. H., Kazi, M., Meza, J. C. & Haranczyk, M. Algorithms and tools for high-throughput geometry-based analysis of crystalline porous materials. *Micropor. Mesopor. Mater.* **149,** 134–141 (2012).
32. Garcia-Perez, E., Dubbeldam, D., Liu, B., Smit, B. & Calero, S. A computational method to characterize framework aluminum in aluminosilicates. *Angew. Chem. Int. Ed.* **46,** 276–278 (2007).
33. Löwenstein, W. The distribution of aluminum in the tetrahedra of silicates and aluminates. *Am. Miner.* **39,** 92–96 (1954).
34. Calero, S. *et al.* Understanding the role of sodium during adsorption. A force field for alkanes in sodium exchanged faujasites. *J. Am. Chem. Soc.* **126,** 11377–11386 (2004).
35. Park, K. S. *et al.* Exceptional chemical and thermal stability of zeolitic imidazolate frameworks. *Proc. Natl Acad. Sci. USA* **103,** 10186–10191 (2006).
36. Garcia-Perez, E. *et al.* A computational study of $CO_2$, $N_2$, and $CH_4$ adsorption in zeolites. *Adsorption-J. Int. Adsorption Soc.* **13,** 469–476 (2007).
37. Garcia-Sanchez, A. *et al.* Transferable force field for carbon dioxide adsorption in zeolites. *J. Phys. Chem. C* **113,** 8814–8820 (2009).
38. Mayo, S. L., Olafson, B. D. & Goddard, W. A. DREIDING—a generic force-field for molecular simulations. *J. Phys. Chem.* **94,** 8897–8909 (1990).
39. Siepmann, J. I. & Potoff, J. J. Vapor-liquid equilibria of mixtures containing alkanes, carbon dioxide, and nitrogen. *Aiche J.* **47,** 1676–1682 (2001).
40. Zhong, C. L. & Xu, Q. A general approach for estimating framework charges in metal-organic frameworks. *J. Phys. Chem. C* **114,** 5035–5042 (2010).
41. Kim, J., Rodgers, J. M., Athenes, M. & Smit, B. Molecular Monte Carlo simulations using graphics processing units: To waste recycle or not? *J. Chem. Theor. Comput.* **7,** 3208–3222 (2011).
42. Bates, S. P., Well, W. J. M. v., Santen, R. A. v. & Smit, B. Energetics of n-alkanes in zeolites: A configurational-bias Monte Carlo investigation into pore size dependence. *J. Am. Chem. Soc.* **118,** 6753–6759 (1996).
43. Haranczyk, M. & Sethian, J. A. Navigating molecular worms inside chemical labyrinths. *Proc. Natl Acad. Sci. USA* **106,** 21472–21477 (2009).
44. Haranczyk, M. & Sethian, J. A. Automatic structure analysis in high-throughput characterization of porous materials. *J. Chem. Theor. Comput.* **6,** 3472–3480 (2010).

## Acknowledgements

The research was supported by the US Department of Energy under contracts DE-AC02-05CH11231, #CSNEW918, DE-SC0001015, DE-FG02-03ER15456, ARPA-e, and CCSI and the Office of Innovation at the Electric Power Research Institute (a detailed description can be found in the Supplementary Information).

## Author contributions

All authors contributed significantly to the work presented in this paper.

## Additional information

The authors declare no competing financial interests. Supplementary information accompanies this paper on www.nature.com/naturematerials. Reprints and permissions information is available online at www.nature.com/reprints. Correspondence and requests for materials should be addressed to B.S.